The Development of a Radial Based Integrated Network for the Modelling of 3D Fused Deposition

AlAlaween, Wafa'; Abueed, Omar; Gharaibeh, Belal; Alalawin, Abdallah; Mahfouf, Mahdi; Alsoussi, Ahmad; Albashabsheh, Nibal

Abstract

Purpose: In this research paper, the fused deposition modelling (FDM) process is investigated and modelled to predict the mechanical attributes of 3D printed specimens. Eight FDM parameters are examined for both Polyether-ether-ketone (PEEK) and Polyether-ketone-ketone (PEKK).

Design/methodology/approach: By exploiting the main effect plots, a Taguchi L18 orthogonal array is employed to investigate the effects of such parameters on three mechanical attributes of the 3D printed specimens. A radial based integrated network is, then, developed to map the eight FDM parameters to the three mechanical attributes for both PEEK and PEKK. Such an integrated network maps and predicts the mechanical attributes through two consecutive phases that consist of several radial basis functions (RBFs).

Findings: Validated on a set of further experiments, the integrated network was successful in predicting the mechanical attributes of the 3D printed specimens. It also outperformed the well-known RBF network with an overall improvement of 24% in the coefficient of

determination. The integrated network is also further validated by predicting the mechanical attributes of a medical-surgical implant (i.e., the MidFace Rim), as an application.

Originality/value: The main aim of this paper is to accurately predict the mechanical properties of parts produced using the FDM process. Such an aim requires modelling a highly dimensional space to represent highly nonlinear relationships. Therefore, a radial based integrated network based on the combination of composition and superposition of radial functions is developed to model FDM using a limited number of data points.

Keywords

Additive manufacturing; Fused deposition modelling; Radial based integrated network; Radial basis function.

Introduction

Additive manufacturing, alternatively referred to as 3D printing and rapid manufacturing/prototyping, is widely recognized as a novel approach in the revolution of sophisticated manufacturing technologies (Conner et al., 2014; Huang, Liu, Mokasdar, & Hou, 2013; Levy, Schindel, & Kruth, 2003). The essence of additive manufacturing is the fabrication of complex 3D objects from previously designed 3D models through the utilization of material additive techniques layer-by-layer or surface-by-surface (Patil, Singh, Raykar, & Bhamu, 2021). Nowadays, additive manufacturing is widely regarded as a critical component of the Industry 4.0 revolution, this being due to (i) its significant impact on the innovation, design and manufacturing processes of the industry; (ii) its remarkable features enabling low-volume manufacturing at inexpensive capital and transportation costs; (iii) its capabilities of producing complicated monolithic geometries;

and (iv) its ability to handle rapid modifications and enable flexible production and mass agility in producing fully customized parts while accommodating wide ranges of sizes, styles, materials and colours (Cano-Vicent et al., 2021; Doshi, Mahale, Singh, & Deshmukh, 2021; Ivanova, Elliott, Campbell, & Williams, 2014; Murr, 2015) . Therefore, there is a surge of research interests and innovation in 3D printing across a broad spectrum of subjects and specialties including, for instance, the aviation and aerospace industries, the pharmaceutical industry and medicine and tissue engineering (Alizadeh-Osgouei, Li, Vahid, Ataee, & Wen, 2021; Boesch, Siadat, Rivette, & Baqai, 2019; Parulski, Jennotte, Lechanteur, & Evrard, 2021; Short, 2015). In general, additive manufacturing is a broad term that encompasses various cutting-edge technologies including fused deposition modelling (FDM), stereolithography (SLA), inkjet printing and selective laser sintering (SLS) (Crump, 1992; Deckard, 1989; Hull, 1986; Sachs, Haggerty, Cima, & Williams, 1993). Among these technologies, FDM, as a nozzle-based system that creates 3D objects by depositing layers of liquefied thermoplastic polymers under a controllable environment, is considered to be the prominent one utilized in various applications, in particular, the biomedical and tissue engineering, where the FDM process can be used to 3D-print biomedical polymers such as Polylactic acid (PLA), Polyether-ether-ketone (PEEK), Polyether-ketone-ketone (PEKK) and Polycaprolactone (D. Singh et al., 2019). Therefore, a considerable research work has been devoted to investigating the FDM process.

Several studies have focused on investigating the applications and the various materials that can be printed using the FDM process for biomedical engineering applications as a substitute for the aggravated and complicated autograft and allograft treatments (D. Singh et al., 2019; S. Singh, Prakash, & Ramakrishna, 2019). For instance, a PLA scaffold was

printed using the FDM process and its properties in terms of mechanical properties, biocompatibility and biodegradability were also examined (D. Singh et al., 2019). In addition, thermal-stimulus-based hydroxyapatite (HA) reinforced PLA scaffolds were produced, and their properties (e.g., biological and mechanical properties and bioactivity) using various FDM parameters were examined (Prakash et al., 2021; G. Singh et al., 2020). Likewise, PLA was amalgamated with nanohydroxyapatite and polyvinyl alcohol in order to improve the mechanical properties of the 3D printed scaffolds without affecting their rheological ones to mimic the actual bone structure (Alizadeh-Osgouei et al., 2021; Esposito Corcione et al., 2017; Song et al., 2018). PEEK and carbon-fiber-reinforced PEEK were also investigated to examine their orthopaedic and dental applications (Dawood, Marti, Sauret-Jackson, & Darwood, 2015).

Many research papers have already addressed the various parameters that determine the quality attributes (e.g., mechanical properties and dimensions) of the 3D printed parts. Such parameters can, in general, be classified into: material-based (e.g., mechanical and rheological properties); operation-based (e.g., temperature, pressure and humidity); and machine-based (e.g., raster angle and deposition flow rate and speed) (Nasereddin, Wellner, Alhijjaj, Belton, & Qi, 2018; Parulski et al., 2021). It is worth mentioning that such parameters need to be carefully identified and optimized to obtain the required quality attributes of the 3D-printed parts. Therefore, many researchers have proposed a wide range of experimental approaches to optimize the FDM parameters (Sheoran & Kumar, 2020). For instance, a comparative analysis was performed to evaluate the combined effects of various polymers and the machine parameters on the mechanical properties of the 3D-printed parts (Khan, Joshi, & Deshmukh, 2021). In addition, statistical analyses (e.g., the

analysis of variance and the correlation coefficient) were employed to investigate the impacts of various parameters (e.g., build orientation, layer thickness, deposition angle, infill type and print speed) on the mechanical properties of the 3D printed parts produced using PLA (Ansari & Kamil, 2021; Carlier et al., 2019; Chacón, Caminero, García-Plaza, & Núnez, 2017; Ouhsti, El Haddadi, & Belhouideg, 2018; Pandzic, Hodzic, & Milovanovic, 2019). Likewise, a 2D digital image correlation was also performed to prove the positive correlation between the PLA specimen thickness and mechanical properties (Xu, Fostervold, & Razavi, 2021).

Various applications, nowadays, require precise and accurate high-quality 3D-printed parts. Therefore, researchers have paid great attention to the development of systematic paradigms that can control the FDM parameters. For example, the VIKOR method, as a multi-criteria decision-making algorithm, was deployed to optimize such parameters (Deomore & Raykar, 2021; Raykar & D'Addona, 2020). Furthermore, the artificial neural network was integrated with the Taguchi method and the genetic algorithm to predict the tensile strength of 3D printed parts produced using different materials (Giri, Shahane, Jachak, Chadge, & Giri, 2021; Pazhamannil, Govindan, & Sooraj, 2021; Teharia, Singari, & Kumar, 2021; Yadav, Chhabra, Garg, Ahlawat, & Phogat, 2020). Moreover, the dimensional analysis conceptual modelling was embedded in the neural network structure to obtain a better understanding of the FDM process and enhance the network generalization capabilities (Nagarajan et al., 2019). In order to intrinsically deal with uncertainties, fuzzy logic was also employed to improve the systematic representation of the FDM process (Trivedi & Gurrala, 2021).

In this research work, the main aim is to accurately predict the mechanical properties of parts produced using the FDM process. This can be attributed to the various applications of FDM, in particular, the medical and tissue-engineering applications that require precise predictions of the properties of the 3D printed parts. Such an aim requires modelling a highly dimensional space to represent highly nonlinear relationships; this being due to the many FDM parameters and their interrelationships that determine the mechanical properties of the 3D printed part. Thus, achieving such an aim requires the acquisition of representative and perhaps large set of data points and/or the development of accurate physical equations which are both considered costly and computationally expensive. Therefore, a radial based integrated network based on the combination of composition and superposition of radial functions is developed to model FDM using a limited number of data points. Therefore, the effects of eight FDM parameters, namely, infill pattern, layer thickness, infill density, print speed, number of shells, cooling-temperature rate, layer orientation and raster width; on the mechanical attributes of the 3D printed specimens produced using PEEK and PEKK are investigated by employing the main effect plots embedded in the Taguchi L18 orthogonal array. A radial based integrated network is, then, developed to extract the input/output relationships and to map the eight FDM parameters to the mechanical attributes in terms of the ultimate tensile strength, elongation and micro-hardness for both PEEK and PEKK. The integrated network is validated on a set of experiments designed using the Taguchi L18 orthogonal array. The elicited model is utilized to predict the mechanical attributes of a medical-surgical implant called the MidFace Rim that is produced using PEEK, as a biocompatible material.

2. Experimental Work

2.1 Experiments and Measurements

In this study, PEEK and PEKK filaments, as high-performance polymers with superior mechanical properties in terms of lubricity, chemical resistance, flexibility and biological stability (Liu, et al,2017), were investigated. Both PEEK and PEKK were supplied by 3DXTECH Additive Manufacturing (Grand Rapids Michigan, USA). ASTM-D638 standard specimens were 3D-printed under different sets of FDM parameters using FUNMAT HT, as a high-temperature functional-materials printer, (INTAMSYS Technology Inc., Minneapolis, USA). Figure 1 shows the FDM printer used in this research work. It is worth mentioning that InstamSuite 3.6.2 software was used to export the 3D models of the designed specimens to a GCODE format for printing. Because of their significant effects on the quality attributes, in particular, the mechanical properties, eight FDM parameters, namely, infill pattern, layer thickness, infill density, print speed, number of shells, cooling-temperature rate, layer orientation and raster width, were examined for both PEEK and PEKK. The levels of such parameters were identified by conducting a set of trial experiments, as summarized in Table 1.

Figure 1. The 3D FUNMAT HT printer.

Table 1. The FDM parameters and their levels and the mechanical properties.

Parameters	Parameters' levels	Mechanical properties
Infill pattern	Cubic and grid	Ultimate tensile strength (MPa)
Layer thickness	0.1, 0.15 and 0.2 µm	Elongation (%)
Infill density	20, 60 and 100%	Micro-hardness
Print speed	10, 30 and 50mm/s	
Number of shells	1, 2 and 3	
Cooling temperature rate	0%, 50% and 100%	
Layer orientation	0°, 45° and 90°	
Raster width	0.25, 0.4 and 0.6µm	

The 3D printing experiments were conducted based on the Taguchi L18 orthogonal array, as a fractional factorial design of experiments, to investigate and model the effects of the parameters on the mechanical attributes while maintaining an equal weight for each one. The Taguchi L18 orthogonal array is summarised in Table 2. A total of 18 experiments were carried-out for each material. Each experiment was repeated three times in order to

examine the repeatability of the measured attributes leading to a total of 54 samples for each material. Once the ASTM-D638 standard specimens were printed and separated from the glass bottom plate, they were left to cool down to room-temperature. All PEKK specimens were annealed as recommended by the manufacturer. The mechanical attributes, in terms of the ultimate tensile strength, elongation and micro-hardness, were measured at room-temperature. The micro Vickers hardness tester (HTMV 2000M, echo LAB, Italy) with a total load of 0.98N and time of 15 seconds was employed to measure the micro-hardness of the 3D-printed specimens by measuring the lengths of the diagonals of the remaining test indentation. Instron (SHIMADZU, USA) allowed for measurements of both the ultimate tensile strength and the elongation with a maximum load of 50KN and speed of 1mm/min. Each measurement was repeated three times and the average was then calculated.

Table 2. Taguchi L18 orthogonal array.

Experiments	Infill pattern	Layer thickness	Infill density	Print speed	Number of shells	Cooling-temperature	layer orientation	Raster width
1	cubic	0.15	60	50	1	0.5	0	0.6
2	grid	0.15	20	10	2	0.5	90	0.6
3	cubic	0.15	20	30	3	0	90	0.4
4	grid	0.2	100	10	3	0.5	0	0.4
5	cubic	0.2	20	50	2	1	0	0.4
6	grid	0.2	60	50	2	0	90	0.25
7	grid	0.15	100	50	1	0	45	0.4
8	cubic	0.15	100	10	2	1	45	0.25
9	grid	0.1	20	10	1	0	0	0.25
10	cubic	0.1	100	30	2	0	0	0.6
11	grid	0.1	100	50	3	1	90	0.6
12	grid	0.1	60	30	2	0.5	45	0.4
13	cubic	0.1	20	50	3	0.5	45	0.25
14	cubic	0.2	100	30	1	0.5	90	0.25
15	cubic	0.2	60	10	3	0	45	0.6
16	grid	0.15	60	30	3	1	0	0.25
17	cubic	0.1	60	10	1	1	90	0.4
18	grid	0.2	20	30	1	1	45	0.6

2.2 Experimental Results

2.2.1 Mechanical Attributes

The ultimate tensile strength, elongation and micro-hardness, as the main mechanical attributes, were measured for the 108 samples for PEEK and PEKK. Various fracture structures (i.e., patterns and locations) were reported. Examples of the fracture structures obtained for various specimens conducted using different sets of printing parameters are shown in Figure 2 (a) for PEEK and Figure 2 (b) for PEKK. It is noticeable that some specimens demonstrated various fracture patterns. In addition, different fracture structures can be seen for the PEEK and PEKK specimens that were conducted using the same set of the FDM parameters.

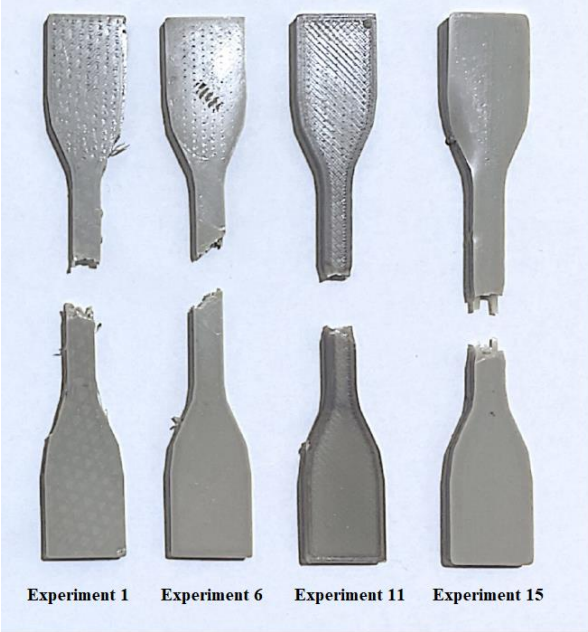

(a)

(b)

Figure 2. Examples of the fracture structures obtained for various (a) PEEK and (b) PEKK specimens.

Figure 3 shows the ultimate tensile strength for the 18 experiments for both PEEK and PEKK. It is also noticeable that, for both materials, the ultimate tensile strength values after

the 3D printing process were lower compared to the ultimate tensile strength values for the PEEK filament (i.e., 100MPa) and the PEKK filament (i.e., 105MPa). This may possibly indicate that the polymer chain arrangements were changed due to the printing and extrusion processes. It is also apparent that the ultimate tensile strength values for PEEK and PEKK follow a similar pattern but with different values. For instance, the ultimate tensile strength values for Experiment 10 were the highest for both PEEK and PEKK, this can be attributed to the high values of the infill density and raster width, and the layer orientation (i.e., the specimens were printed horizontally with a zero angle). The ultimate tensile strength values for Experiment 9 were the minimum, this being due to mainly the low values of the infill density and raster width. For Experiments 8 and 14, the ultimate tensile strength values for PEEK were three and two times that for PEKK, respectively. This can be attributed to the fact that PEKK, as a semi-crystalline material having an additional ketone group, has relatively high thermal and chemical resistance attributes, which were significantly affected by both the differences in the temperature-cooling rate and the layer thickness in these experiments, as presented in Table 2. This may be the same reason behind the high ultimate tensile strength for PEKK for Experiment 13.

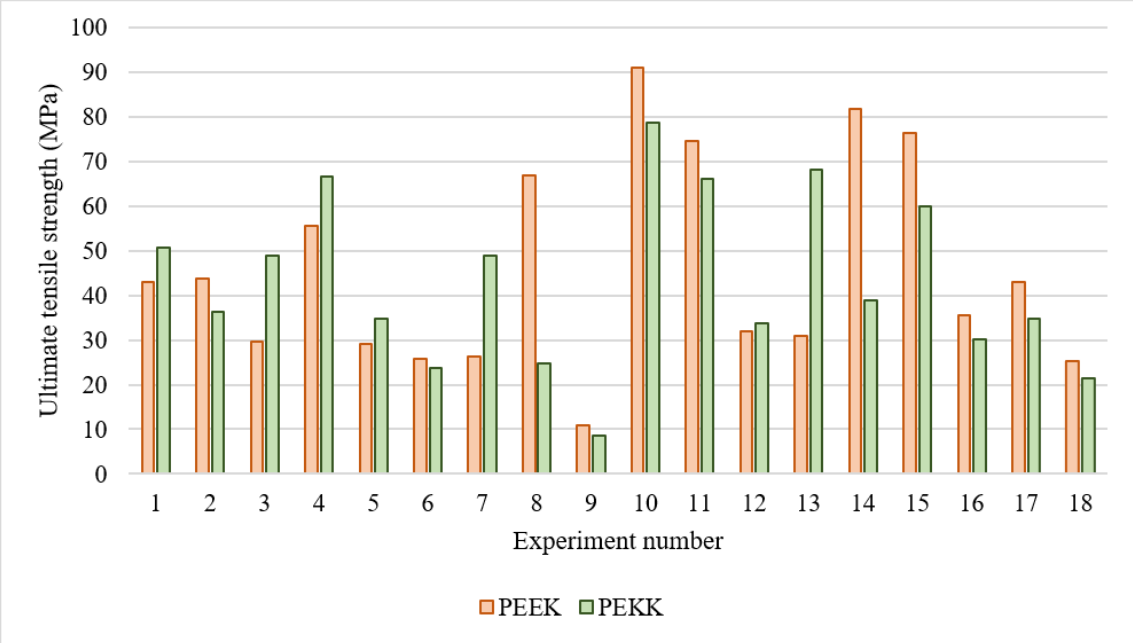

Figure 3. The ultimate tensile strength for the 18 experiments for PEEK and PEKK.

Figure 4 shows the elongation for the 18 experiments for both PEEK and PEKK. It is apparent that the elongation percentages after the 3D printing process were higher compared to the elongation percentages for the PEEK filament (i.e., 20%) and the PEKK filament (i.e., 5%). This indicates that the 3D printing process and its parameters enhanced the ductility of both materials. For instance, the highest elongation percentage for PEEK was for Experiment 18, such a value was three times that for the PEKK. This can be attributed to the high value of the raster width, which has a direct relationship with the elongation percentage for PEEK but an inverse relationship with the elongation percentage for PEKK. Such relationships can also be proven by close examination of the elongation percentages for both PEEK and PEKK for Experiment 16, where the low value of the raster width has increased the elongation percentage for PEKK to be more than two times of it for PEEK. It is also noticeable that the minimum elongation percentages for both PEEK

and PEKK were for Experiment 7, this being due to the high value of the infill pattern that has negatively affected the elongation percentages for the two materials.

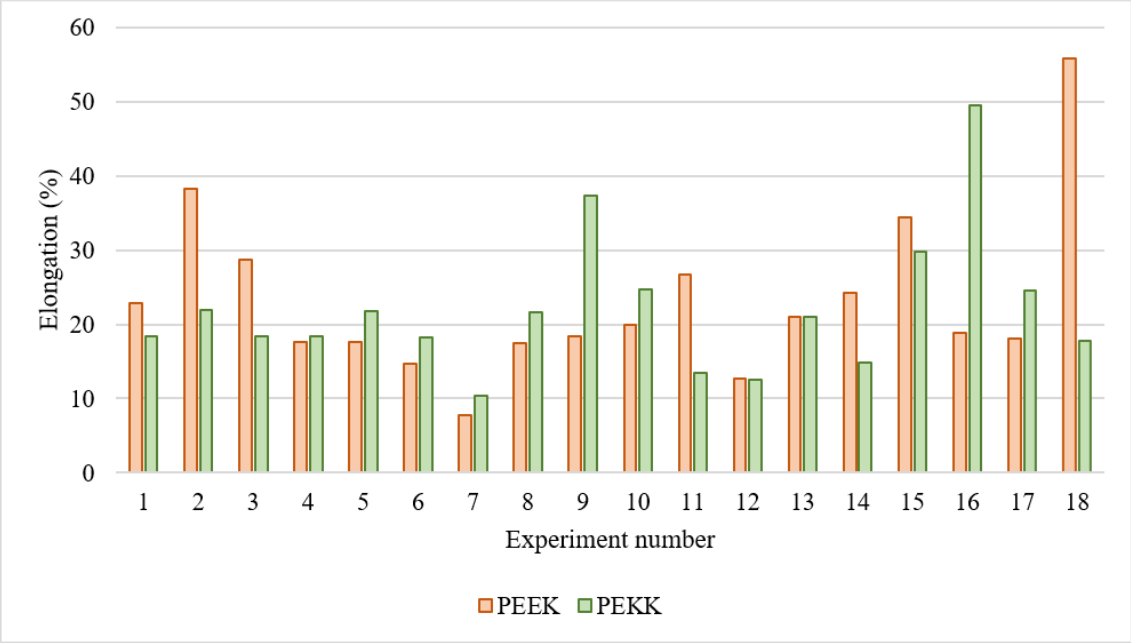

Figure 4. The elongation for the 18 experiments for PEEK and PEKK.

Figure 5 shows the micro-hardness values for the 18 experiments for both PEEK and PEKK. In contrast to the ultimate tensile strength and the elongation percentages, the difference in the micro-hardness values between PEEK and PEKK is not significant for the majority of the experiments. However, the micro-hardness values for Experiments 8 and 9 for PEEK are higher than that for PEKK. This can be attributed to the values of the infill density and the layer orientation. Whereas the micro-hardness values for Experiments 6 and 7 for PEKK are higher than that for PEEK, this being due to the value of the raster width.

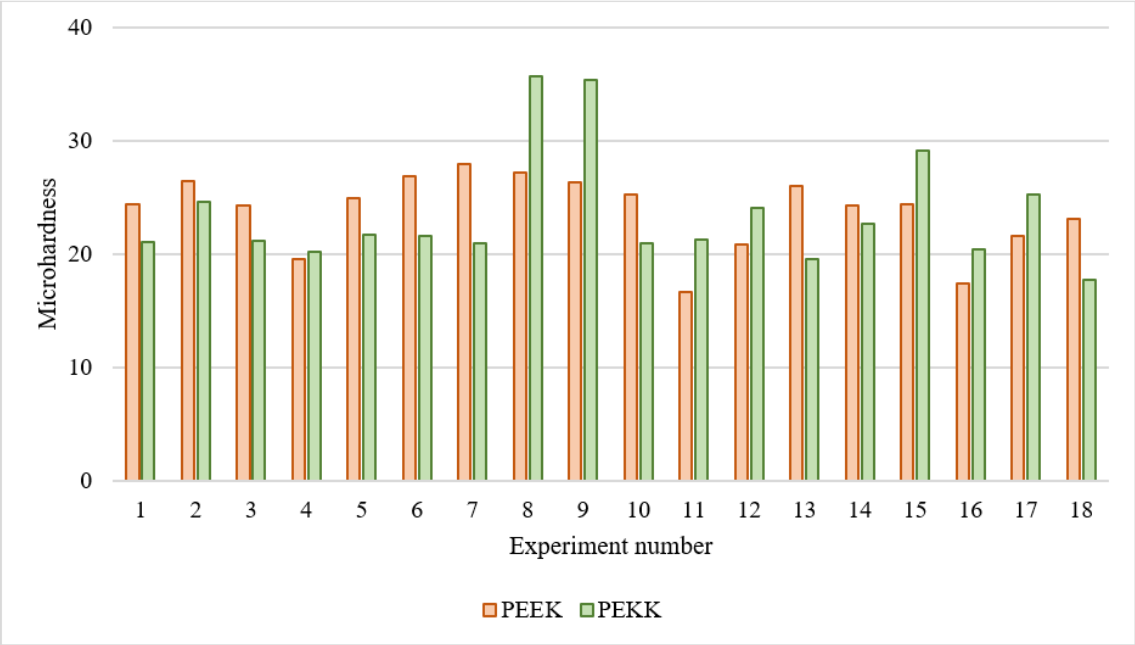

Figure 5. The micro-hardness values for the 18 experiments for PEEK and PEKK.

2.2.2 Main Effects Analysis

To statistically analyse the significant effects of the eight investigated parameters, the main effect plots were investigated for each material. Figure 6 depicts the main effects of the eight parameters on the three mechanical attributes for PEEK. The results reveal that the cooling-temperature rate and the layer orientation have slightly affected the ultimate tensile strength, whereas the layer thickness, print speed and the number of shells have significantly affected the ultimate tensile strength. It is apparent that the print speed has, for instance, an inverse relationship with the ultimate tensile strength with a slight variation between 10 and 30mm/s levels. Furthermore, the infill density, infill pattern and raster width have significantly influenced the ultimate tensile strength, where a cubic infill pattern, an infill density of 100% and a raster width of 0.6µm have shown a considerably high effect on the ultimate tensile strength. For the elongation, the results indicate that the

layer thickness, infill density, print speed and raster width have significantly influenced the elongation percentage, where a layer thickness of 0.2μm, an infill density of 20% and a raster width of 0.6μm have led to the maximum elongation percentage. Similarly to the ultimate tensile strength, the print speed has an inverse relationship with the elongation percentage. It is also worth noting that a raster width of 0.4μm has slightly decreased both the ultimate tensile strength and the elongation percentage. For the micro-hardness, it is evident that the infill pattern, number of shells and cooling-temperature rate have significant effects on the micro-hardness values of the PEEK specimens, where the minimum micro-hardness value was obtained when high values of the infill density, number of shells and cooling-rate temperature and a low value of the layer thickness were used. In contrast to the ultimate tensile strength and elongation, the print speed, for instance, has an inverse relationship with the micro-hardness values at low values of the print speed and then a direct relationship at high values of the print speed. Such a behaviour was also noticed for many parameters.

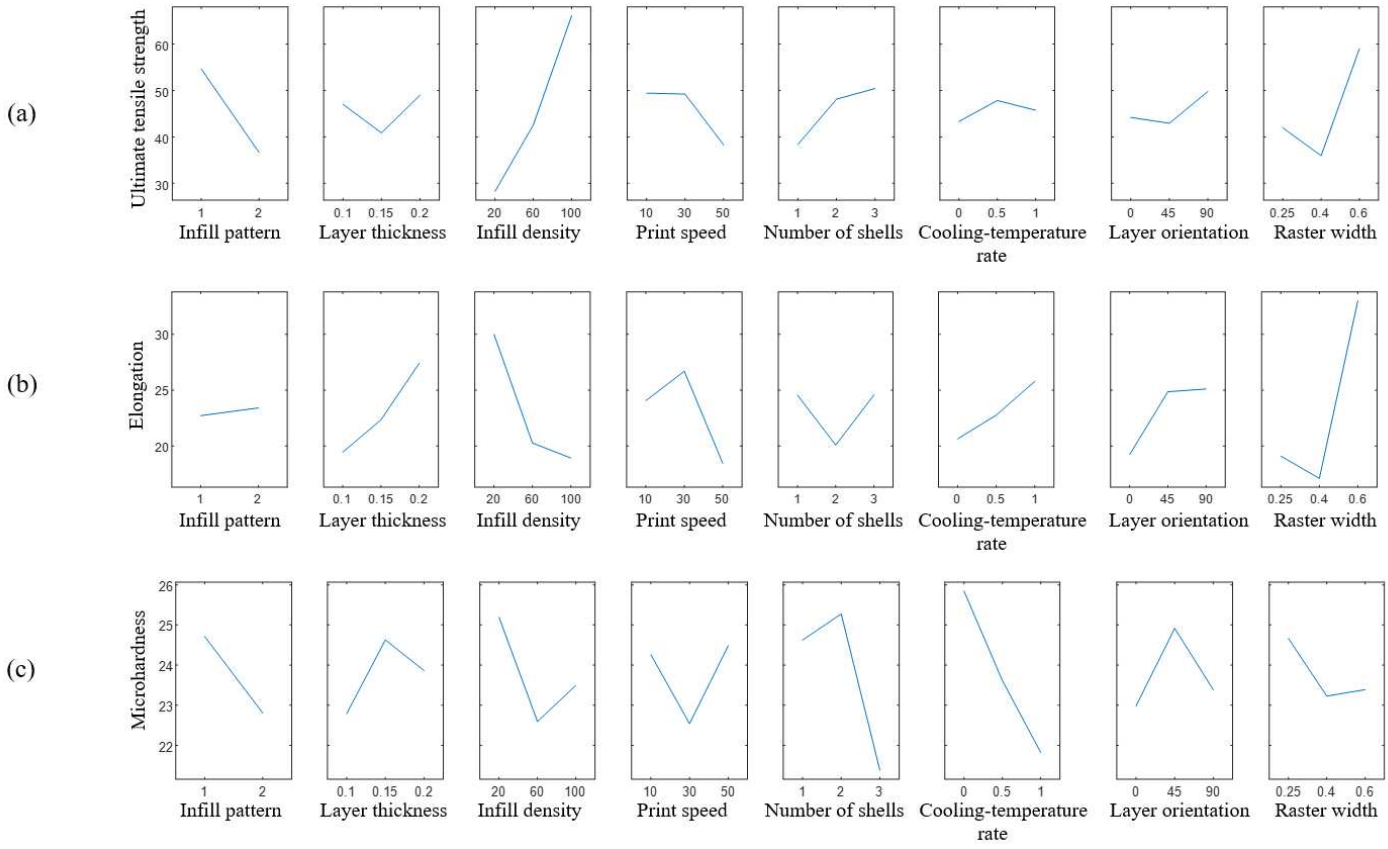

Figure 6. The main effect of the eight parameters on the (a) Ultimate tensile strength; (b) Elongation percentage; and (c) Micro-hardness for PEEK (Infill pattern 1 is for cubic and 2 is for grid).

In a similar manner, the main effects of the eight parameters on the three mechanical attributes for PEKK are presented in Figure 7. From this figure, it is evident that the layer thickness, print speed and cooling-temperature rate have considerable effects on the ultimate tensile strength, whereas the layer orientation has a negligible effect on it. In addition, the infill density and pattern, the number of shells and raster width have significant effects on the ultimate tensile strength. In contrast to PEEK, a direct relationship

can be noted between the print speed and the ultimate tensile strength for PEKK. In addition, a raster width of 0.4μm has a direct effect on the ultimate tensile strength for PEKK but an inverse one on it for PEEK. For the elongation, low values of the layer orientation (i.e., printing horizontally), raster width and print speed can significantly increase the elongation of PEKK (i.e., increasing the ductility). Whereas both the layer thickness and infill density have inclined to follow a distinct pattern compared to the PEEK pattern. For the micro-hardness, the print speed, number of shells and raster width have significantly influenced the values of the micro-hardness, whereas the infill pattern and infill density have negligible effects on the micro-hardness values for PEKK. Unlike the ultimate tensile strength and similarly to the elongation percentage, the print speed has an inverse relationship with the micro-hardness of PEKK. In addition, such an inverse relationship with the micro-hardness values leads to a significant variation between 10 and 30mm/s levels, but almost a negligible variation between 30 and 50mm/s levels. In contrast to PEEK, the print speed has an inverse relationship with the micro-hardness values.

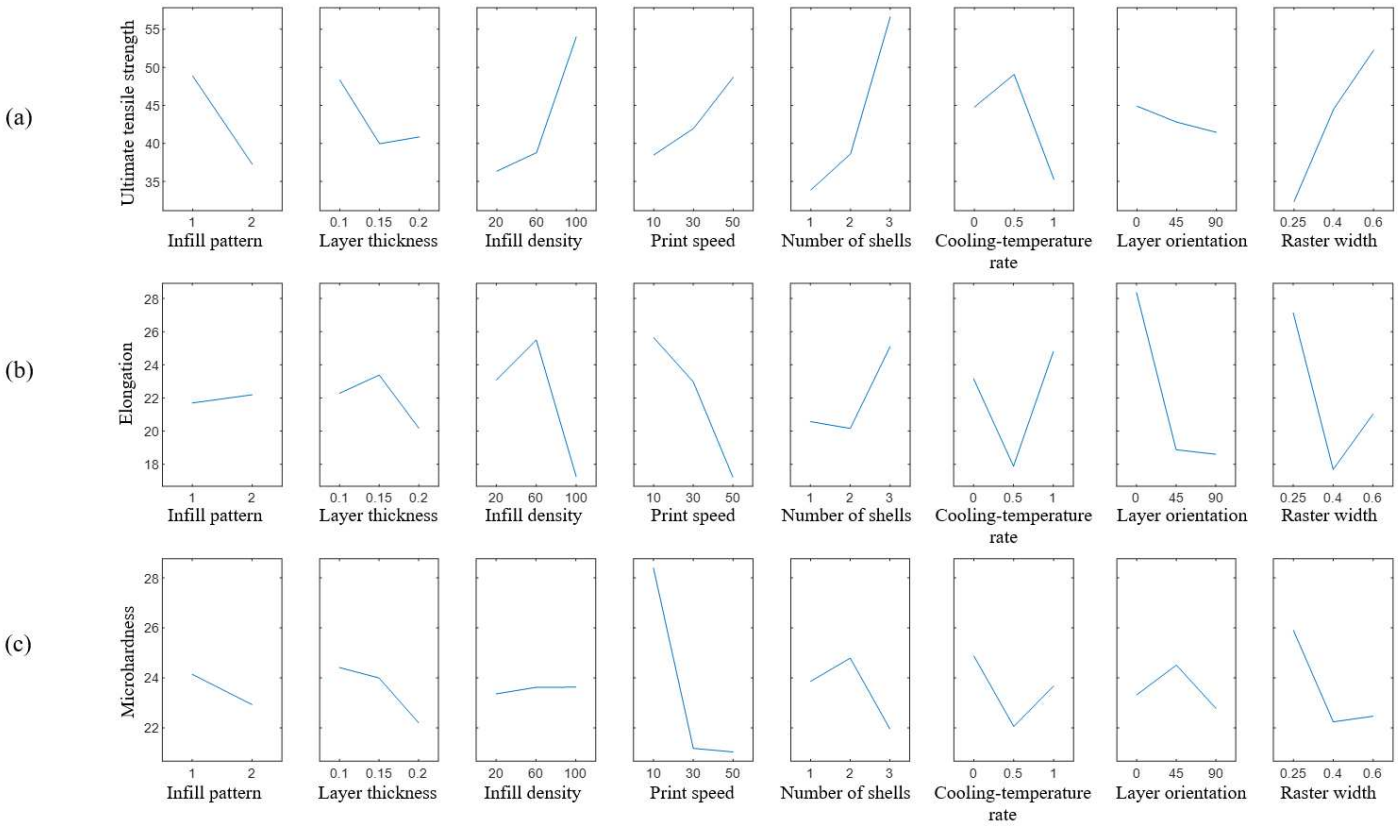

Figure 7. The main effect of the eight parameters on the (a) Ultimate tensile strength; (b) Elongation percentage; and (c) Micro-hardness for PEKK (Infill pattern 1 is for cubic and 2 is for grid).

3. Models Development

3.1 Radial Basis Function Network

Recently, data-driven modelling paradigms have been employed in various areas including marine, metallurgy and pharmaceutics (AlAlaween et al., 2022; AlAlaween, Mahfouf, & Salman, 2021). Such models are usually developed by using observed/experimental data that can complement/replace physical-driven paradigms (AlAlaween, Mahfouf, & Salman, 2017). Because of its proven effectiveness and flexibility, the radial basis function (RBF)

network has been utilized in a variety of applications (e.g., engineering and health) (Alshafiee et al., 2019). Figure 8 shows a schematic representation of the RBF network. Such a network comprises of three layers: an input layer that represents the inputs space; basis function where the network calculations take place; and an output layer that represents the output space. Therefore, the RBF network maps an input space that consists of several vectors ($\mathbf{x}=x_1, x_2, \ldots, x_n$) through the basis functions ($\xi_i(\mathbf{x})$) to an output space (y) for a multi-input single-output (MISO) space.

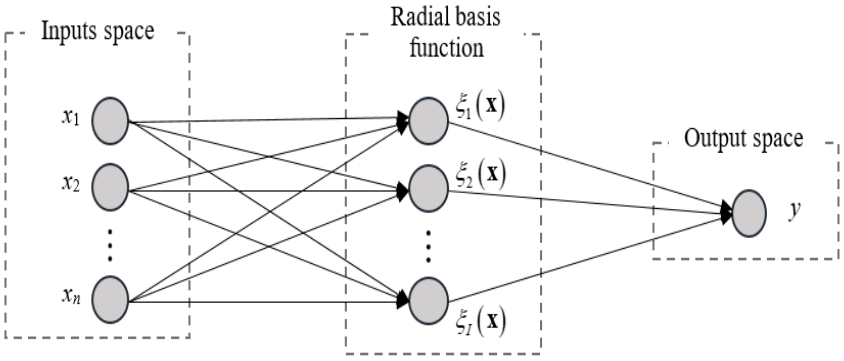

Figure 8. The radial basis function network.

In general, basis functions depend on the distance measured commonly as the Euclidian distance from a predefined and optimized centre. Various types of basis functions can be utilized including, for instance, polyharmonic spline and bump functions (Bishop & Nasrabadi, 2006). Because of its effectiveness and approximation ability, the Gaussian function is employed in this research work. The Gaussian function can be mathematically expressed as follows (AlAlaween, Khorsheed, Mahfouf, Reynolds, & Salman, 2020):

$$\xi_i(\mathbf{x}) = \exp\left(-\frac{(x-\mu_i)^2}{2\sigma_i^2}\right) \tag{1}$$

where μ_i and σ_i represent the parameters in terms of the mean and standard deviation of the i^{th} Gaussian function, respectively. The predicted output (y_P) of the RBF network can then be written as a linear combination of such functions as follows (Alshafiee et al., 2019):

$$y_p(\mathbf{x}) = \sum_{i=1}^{I} \lambda_i \xi_i(\mathbf{x}) + \lambda_o \quad (2)$$

where λ_o and λ_i represent the bias and the weight of the i^{th} Gaussian function, respectively. Such parameters are usually initialized randomly and, then, optimized using the back-propagation network. Commonly, various optimization algorithms (e.g., conjugate gradient and Levenberg-Marquardt) can be embedded in the back-propagation network to optimize the basis function parameters (Bishop & Nasrabadi, 2006). Because of its relatively fast convergence property, the scaled conjugate gradient algorithm, as a supervised algorithm, was employed in this research work. The number of basis functions in an RBF network cannot be determined in advance unlike the numbers of neurons in the input and the output layers which are usually defined according to the case investigated. Therefore, the number of basis functions in an RBF network is optimized by minimizing the predictive error and obtaining acceptable generalization capabilities (AlAlaween et al., 2021; Bishop & Nasrabadi, 2006). In this research work, both the coefficient of determination (R^2) and the root mean square error (RMSE) for the training and the testing data sets were employed as measures for the minimum predictive error and acceptable generalization capabilities.

3.2 Integrated Network

In general, the core of the data-driven paradigms relies on the data provided, in other words, the performance of such models depends on the data. For instance, sparse data may lead to a biased model that performs accurately in the areas where the data are sufficient and

inaccurately elsewhere. Therefore, in the majority of the cases, the lack of representative data is one of the main challenges associated with the development of data-driven models, and the representation of the relationships between the inputs and the outputs (AlAlaween, Mahfouf, & Salman, 2016). Therefore, an integrated network structure is utilized to develop a model that can be dense in a convex space and, therefore, can extract the information hidden in a provided data set. The main idea of the integrated network is to extract information from the data provided by training a number of models in two phases. In Phase I, the process inputs and the output are employed to develop a number of models. The predicted outputs from these models are then mapped to the process output by developing another model in Phase II in order to obtain the final predicted output.

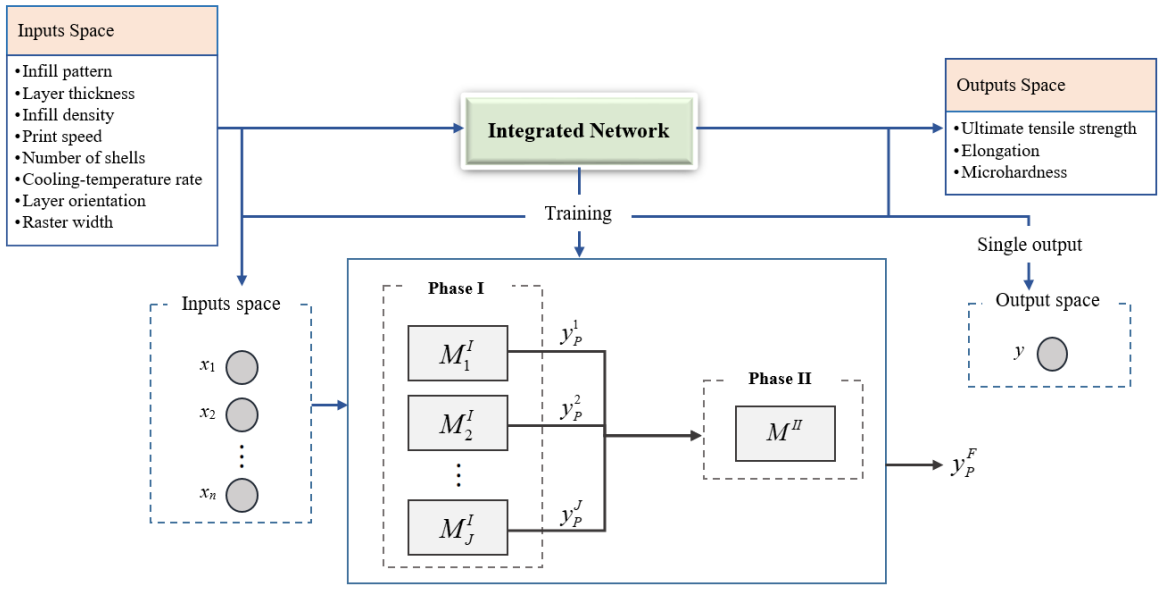

Figure 9. The schematic diagram of the integrated network.

Figure 9 presents the schematic structure of the integrated network for an MISO system. In Phase I, an input space that consists of N vectors ($\mathbf{x}=x_1, x_2, \ldots, x_n$) and an output space (y), which represents the actual/experimental output, are employed to train J data-driven

models. The models in Phase I can be different in terms of their structures and parameters. In Phase II, the predicted outputs of the *J* models (y_p^j) are mapped to the output space to determine the final predicted output (y_p^F) of the integrated network by developing a linear/nonlinear model. The models in Phases I and II with their different structures and parameters can play a complementary role in capturing and, thus, representing the complex relationships between the input and the output spaces (AlAlaween et al., 2016). In addition, the information required can be extracted in the two phases by training the data through such phases.

In this research work, the RBF model, as an efficient and flexible model, is included in Phases I and II. Using the mathematical expression of the RBF model presented in Section 3.1, the mathematics behind the integrated network can be analytically represented as follows (AlAlaween et al., 2016):

$$y_p^F\left(\mathbf{x}\right)=\sum_{j=1}^{J}\lambda_j^{II}\,\xi_j\left(\sum_{i=1}^{I}\lambda_i\xi_i\left(\mathbf{x}\right)+\lambda_o\right)+\lambda_o^{II} \tag{3}$$

the parameters in such an equation are as defined in Section 3.1. Since the RBF model is used in the second phase, the superscript (II) is utilized to distinguish Phase II parameters. The mathematical equation of the integrated network presents its predicted output as a combination of composition and superposition of the Gaussian functions (i.e., basis function). Such a combination has been proved to be dense in a convex space (Cybenko, 1988; MATELJEVH & PAVLovré, 1995). The number of the models (*J*) in Phase I can play a significant role in the integrated network. This is represented by the inner sum shown in Equation (3) which expresses the superposition of the Gaussian functions. Therefore, the predictive performance of the integrated network is expected to be better as the

difference between the predicted values and the target ones is expected to be smaller when the parameters of each model in both phases are optimized as discussed in Section 3.1. In this research work, the parameters were optimized using the scaled conjugate gradient (SCG) algorithm that is integrated with the backpropagation network (Bishop & Nasrabadi, 2006).

4. Results and Discussion

4.1 Radial Basis Function Network

Three RBF networks were developed to map the input space that consists, in addition to the material type, of the eight parameters listed in Table 1, to the outputs space that consists of the ultimate tensile strength, elongation and micro-hardness of the 3D-printed specimens. It is worth mentioning at this stage that an RBF network was developed for each output. For each output, the RBF model was developed by randomly classifying the experimental data into two sets: training (28) and testing (8) sets that were used to identify the input/output relationships and to test the RBF generalization capabilities, respectively. Various numbers of basis functions in the range of 1 to 15 were tested. The best number of the basis functions that was finally selected was the one that led to the best RBF network, which has the minimum RMSE and, thus, has the best predictive performance. For the ultimate tensile strength, Figure 10 shows the RBF predictive performance for the training and the testing data sets using 7 basis functions. The predictive performance measures are RMSE (training, testing) = [8.3, 10.7] and R^2 (training, testing) = [0.83, 0.79], as summarized in Table 3. It is noticeable that approximately 11 points out of 28 and 5 points out of 8 in the training and testing sets, respectively, fall outside the 90% confidence

interval level. In addition, such points are sparsely distributed around the best-fit line. In addition to the predictive performance measures, this indicates that the RBF model was not able to successfully map the ultimate tensile strength to the 3D-printing parameters investigated in this research work for both PEEK and PEKK. This can be attributed to the limited number of experiments available and to the number of parameters investigated which could lead to the well-known phenomenon of the "curse of dimensionality" (Bishop & Nasrabadi, 2006).

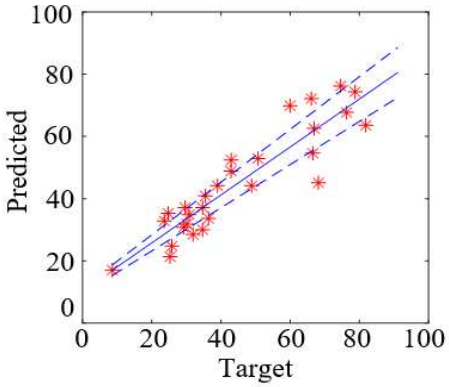

(a)

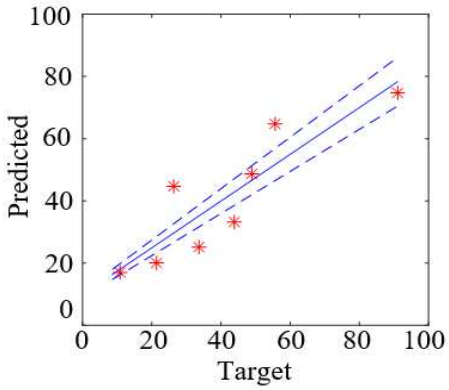

(b)

Figure 10. The RBF predictive performance for the ultimate tensile strength with a 90% confidence level.

Table 3. The performance measures of the integrated network and the radial basis function network.

Model	RBF				Integrated Network			
	R^2		RMSE		R^2		RMSE	
Output	Training	Testing	Training	Testing	Training	Testing	Training	Testing
Ultimate tensile strength	0.83	0.79	8.3	10.7	0.94	0.91	5.4	5.9
Elongation	0.72	0.76	5.9	4.0	0.93	0.91	2.3	7.6
Micro-hardness	0.68	0.69	2.8	2.9	0.90	0.91	1.3	1.4

In a similar manner, RBF networks were also developed for the elongation and the micro-hardness. The performance measures in terms of the RMSE and R^2 for such outputs are summarized in Table 3. From the latter, it is evident that the performance measures of the RBF model for the examined mechanical attributes were not as expected. In addition, the performance measures for the micro-hardness were lower than that for the ultimate tensile strength and elongation. In addition to the limited number of experiments and the highly dimensional space, this can be attributed to the uncertainties in measuring the micro-hardness of the 3D printed specimens due to the surface texture. Therefore, the RBF performance measures can be improved by reducing the dimensionality of the inputs space (i.e., reducing the number of input parameters investigated) or by employing a model that can be dense in the space investigated. Therefore, an integrated network was employed in this research paper to map the inputs space to the mechanical properties of the 3D printed specimens.

4.2 Integrated Network

Three integrated networks based on ten (10) RBF networks in Phase I and an RBF network in Phase II were developed. An integrated network was developed for each mechanical property. For each RBF network in Phase 1, the experimental data were randomly divided

into training (28) and testing (8) sets. Although the numbers of experiments in the two sets for all the models in Phase I were the same, their distributions were different. This can lead to different RBF networks that can play complementary roles in extracting the patterns and mapping the inputs space to the output space. It is worth mentioning that the mean and standard deviation of the basis functions were initially identified using the K-means clustering, whereas the weights were randomly initialised. The scaled conjugate gradient algorithm was then employed to optimize the RBF parameters. In a similar manner, an RBF network was developed in Phase II based on the outputs of the RBF networks developed in Phase I. The inputs of the RBF network in the second phase were the predictive outputs of the ten RBF networks in the first phase. The performance of the integrated network for the ultimate tensile strength is shown in Figure 11. The predictive performance measures are RMSE (training, testing) = [5.4, 5.9] and R^2 (training, testing) = [0.94, 0.91], as summarized in Table 3. From this latter, it is apparent that the majority of the points fall within the 90% confidence interval and they are distributed nicely around the best-fit line. For the ultimate tensile strength, the predictive performance measures of the integrated network showed that the integrated network outperformed the RBF network with an overall improvement of 13.7% in R^2. In addition, the integrated network was able to extract the patterns of the data and map the highly dimensional inputs space to the output space that consisted of the ultimate tensile strength.

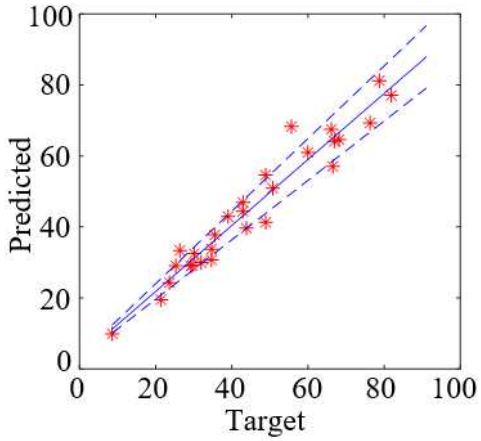

(a)

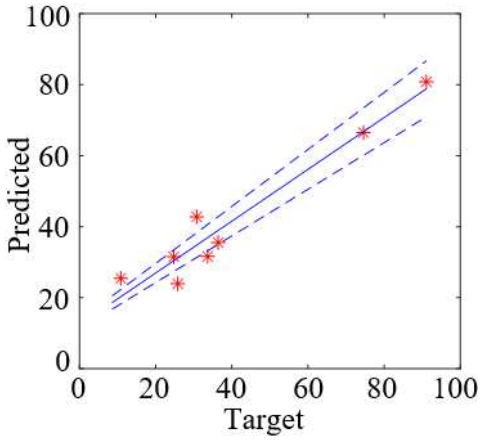

(b)

Figure 11. The integrated network predictive performance for the ultimate tensile strength with a 90% confidence level.

In a similar manner, integrated networks were also used to map the elongation and the micro-hardness of the 3D printing specimens to the inputs space. The performance measures in terms of RMSE and R^2 for the elongation and the micro-hardness are presented in Table 3. For the elongation, it is apparent that the RMSE value for the testing set is approximately three times the RMSE value for the training set. This may indicate that the

model generalization capabilities were not satisfactory. However, this is not the case in this research work as presented in Figure 12, which shows the predictive performance of the integrated network for the elongation. The high RMSE value was due to the actual values of the elongation, where one point out of 8 in the testing set has a value of more than 50%. The RMSE value for such a point was relatively high, however, it is less than the 10% error. This can be proved by estimating the values of the R^2 for both the training and testing sets. Such values presented in Table 3 are very close and the difference between them is almost negligible which indicates that the model generalization capabilities are as expected. In a similar manner, the predictive performance of the integrated network for the micro-hardness is presented in Figure 13. From this figure, it is apparent that the majority of the data points fall within the 90% confidence interval. In addition, the performance measures of the integrated network for the micro-hardness are RMSE (training, testing) = [1.3, 1.4] and R^2 (training, testing) = [0.90, 0.91], as summarized in Table 3. Such performance measures show that the integrated network was able to represent the input/output relationships and to extract the possible patterns from the experimental data available. Likewise, Table 3 shows that, for all the mechanical attributes, the integrated network outperformed the RBF network, this being due to the structure of the integrated network that can map a highly dimensional inputs space to an output space by extracting input/output patterns using a limited number of data points.

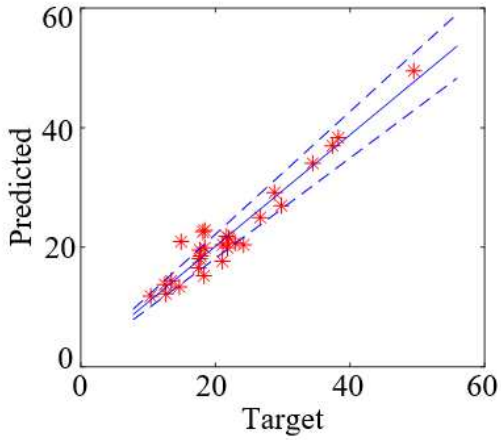

(a)

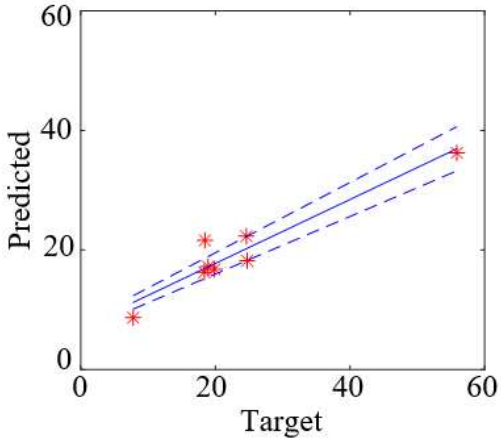

(b)

Figure 12. The integrated network predictive performance for the elongation with a 90% confidence level.

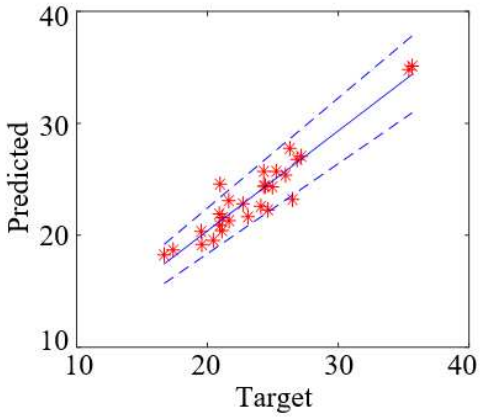

(a)

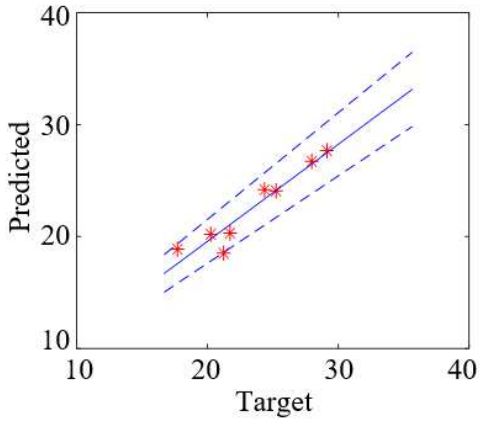

(b)

Figure 13. The integrated network predictive performance for the elongation with a 90% confidence level.

4.3 Model Validation: A Medical Application

To prove the ability of the integrated network in predicting the mechanical properties of the 3D-printed parts, the MidFace Rim, as a medical-surgical implant, shown in Figure 14, was produced using the FDM 3D printer and its mechanical properties were predicted using the integrated networks. It is worth emphasizing at this stage that measuring some of the

mechanical attributes such as the ultimate tensile strength for a specimen that is not designed as the standard tensile test specimens may not be as accurate and as straightforward as would be expected. Therefore, the developed integrated network can be used in such a case and, perhaps, similar cases to predict the mechanical attributes of medical implants. The printing variables that were used to print the MidFace Rim using PEEK, as a biocompatible material, were: cubic infill pattern, a layer thickness of 0.12µm, an infill density of 100%, a print speed of 20mm/s, a number of shells of 3, a cooling-temperature rate of 0%, a layer orientation of 0° and a raster width of 0.4µm. The predicted values of the ultimate tensile strength, elongation and micro-hardness of such a part by using the developed integrated networks presented in Section 4.2 are 100.6MPa, 20.8 and 28.7, respectively. The micro-hardness was measured for the MidFace Rim at different points. The micro-hardness values were 28.62, 31.74 and 31.17. The average of such values was 30.5, which is comparable to the predicted value (i.e., 28.7). This can prove the ability of the integrated network in predicting the mechanical attributes of the 3D printed parts.

Figure 14. The MidFace Rim part.

5. Conclusions

The fused deposition modelling (FDM) was investigated and modelled in this research work. For both Polyether-ether-ketone (PEEK) and Polyether-ketone-ketone (PEKK), the effects of eight FDM parameters on three mechanical attributes were investigated by embedding the main effect plots in the Taguchi L18 orthogonal array. The FDM process was then modelled by developing a radial based integrated network to map the eight FDM parameters to the three mechanical attributes. Validated on a set of experiments, the integrated network was able to successfully predict the mechanical attributes of the 3D printed specimens. Furthermore, the integrated network was able to capture the input/output relationships in the highly-dimensional space investigated. It also outperformed the radial basis function network with an overall improvement of 24% in the coefficient of determination. Furthermore, the integrated network was also utilized to predict the mechanical attributes of a medical-surgical implant called the MidFace Rim that was produced using PEEK. In summary, accurately predicting the mechanical attributes of 3D printed parts produced using the FDM presents a promising development in the additive manufacturing, as manufacturers can predict and also control the attributes of 3D printed parts that are used in many applications, in particular, the medical area. However, there is a strong need to enhance the interpretability of the FDM, and to deal with measurement uncertainties. Therefore, it can be advantageous to incorporate the fuzzy logic with the integrated network to enable users to (i) extract and represent the relationships linguistically; and (ii) deal with uncertainties, in particular, measurement uncertainties that affected the modelling performance of the models developed for the mechanical attributes (e.g., micro-hardness).

References

AlAlaween , W. H., AlAlawin, A. H., Mahfouf, M., Abdallah, O. H., Shbool, M. A., & Mustafa, M. F. (2021). A new framework for warehouse assessment using a Genetic-Algorithm driven analytic network process. *PLOS ONE, 16*(9), 1-16.

AlAlaween, W. H., Faouri, N. M., Al-Omar, S. H., Hendaileh, E. M., Almousa, A. S. S., AlAlawin, A. H., . . . Abueed, O. A. (2022). A dynamic nonlinear autoregressive exogenous model for the prediction of COVID-19 cases in Jordan. *Cogent Engineering, 9*(1), 2047317.

AlAlaween, W. H., Khorsheed, B., Mahfouf, M., Reynolds, G. K., & Salman, A. D. (2020). An interpretable fuzzy logic based data-driven model for the twin screw granulation process. *Powder Technology, 364*, 135-144.

AlAlaween, W. H., Mahfouf, M., & Salman, A. D. (2016). Predictive modelling of the granulation process using a systems-engineering approach. *Powder Technology, 302*, 265-274.

AlAlaween, W. H., Mahfouf, M., & Salman, A. D. (2017). Integrating the physics with data analytics for the hybrid modeling of the granulation process. *AIChE Journal, 63*(11), 4761-4773.

AlAlaween, W. H., Mahfouf, M., & Salman, A. D. (2021). When swarm meets fuzzy logic: Batch optimisation for the production of pharmaceuticals. *Powder Technology, 379*, 174-183.

Alizadeh-Osgouei, M., Li, Y., Vahid, A., Ataee, A., & Wen, C. (2021). High strength porous PLA gyroid scaffolds manufactured via fused deposition modeling for tissue-engineering applications. *Smart Materials in Medicine, 2*, 15-25.

Alshafiee, M., AlAlaween, W. H., Markl, D., Soundaranathan, M., Almajaan, A., Walton, K., . . . Asare-Addo, K. (2019). A predictive integrated framework based on the radial basis function for the modelling of the flow of pharmaceutical powders. *International journal of pharmaceutics, 568*, 118542.

Ansari, A. A., & Kamil, M. (2021). Effect of print speed and extrusion temperature on properties of 3D printed PLA using fused deposition modeling process. *Materials Today: Proceedings, 45*, 5462-5468.

Bishop, C. M., & Nasrabadi, N. M. (2006). *Pattern recognition and machine learning* (Vol. 4): Springer.

Boesch, E., Siadat, A., Rivette, M., & Baqai, A. A. (2019). Impact of fused deposition modeling (FDM) process parameters on strength of built parts using Taguchi's design of experiments. *The international journal of advanced manufacturing technology, 101*(5), 1215-1226.

Cano-Vicent, A., Tambuwala, M. M., Hassan, S. S., Barh, D., Aljabali, A. A., Birkett, M., . . . Serrano-Aroca, Á. (2021). Fused deposition modelling: Current status, methodology, applications and future prospects. *Additive Manufacturing, 47*, 102378.

Carlier, E., Marquette, S., Peerboom, C., Denis, L., Benali, S., Raquez, J., . . . Goole, J. (2019). Investigation of the parameters used in fused deposition modeling of poly (lactic acid) to optimize 3D printing sessions. *International Journal of Pharmaceutics, 565*, 367-377.

Chacón, J., Caminero, M. A., García-Plaza, E., & Núnez, P. J. (2017). Additive manufacturing of PLA structures using fused deposition modelling: Effect of process parameters on mechanical properties and their optimal selection. *Materials & Design, 124*, 143-157.

Conner, B. P., Manogharan, G. P., Martof, A. N., Rodomsky, L. M., Rodomsky, C. M., Jordan, D. C., & Limperos, J. W. (2014). Making sense of 3-D printing: Creating a map of additive manufacturing products and services. *Additive Manufacturing, 1*, 64-76.

Crump, S. S. (1992). Apparatus and method for creating three-dimensional objects. In: Google Patents.

Cybenko, G. (1988). *Continuous valued neural networks with two hidden layers are sufficient*: University of Illinois at Urbana-Champaign. Center for Supercomputing Research

Development.
Dawood, A., Marti, B. M., Sauret-Jackson, V., & Darwood, A. (2015). 3D printing in dentistry. *British dental journal, 219*(11), 521-529.
Deckard, C. R. (1989). Method and apparatus for producing parts by selective sintering. In: Google Patents.
Deomore, S. A., & Raykar, S. J. (2021). Multi-criteria decision making paradigm for selection of best printing parameters of fused deposition modeling. *Materials Today: Proceedings, 44*, 2562-2565.
Doshi, M., Mahale, A., Singh, S. K., & Deshmukh, S. (2021). Printing parameters and materials affecting mechanical properties of FDM-3D printed Parts: Perspective and prospects. *Materials Today: Proceedings*.
Esposito Corcione, C., Gervaso, F., Scalera, F., Montagna, F., Sannino, A., & Maffezzoli, A. (2017). The feasibility of printing polylactic acid–nanohydroxyapatite composites using a low-cost fused deposition modeling 3D printer. *Journal of Applied Polymer Science, 134*(13).
Giri, J., Shahane, P., Jachak, S., Chadge, R., & Giri, P. (2021). Optimization of FDM process parameters for dual extruder 3d printer using Artificial Neural network. *Materials Today: Proceedings, 43*, 3242-3249.
Huang, S. H., Liu, P., Mokasdar, A., & Hou, L. (2013). Additive manufacturing and its societal impact: a literature review. *The International Journal of Advanced Manufacturing Technology, 67*(5), 1191-1203.
Hull, C. W. (1986). Apparatus for production of three-dimensional objects by stereolithography. In: Google Patents.
Ivanova, O., Elliott, A., Campbell, T., & Williams, C. (2014). Unclonable security features for additive manufacturing. *Additive Manufacturing, 1*, 24-31.
Khan, S., Joshi, K., & Deshmukh, S. (2021). A comprehensive review on effect of printing parameters on mechanical properties of FDM printed parts. *Materials Today: Proceedings*.
Levy, G. N., Schindel, R., & Kruth, J.-P. (2003). Rapid manufacturing and rapid tooling with layer manufacturing (LM) technologies, state of the art and future perspectives. *CIRP annals, 52*(2), 589-609.
MATELJEVH, M., & PAVLovré, M. (1995). The best approximation and composition with inner functions. *Michigan Math. J, 42*, 367.
Murr, L. (2015). Metallurgy of additive manufacturing: Examples from electron beam melting. *Additive Manufacturing, 5*, 40-53.
Nagarajan, H. P., Mokhtarian, H., Jafarian, H., Dimassi, S., Bakrani-Balani, S., Hamedi, A., . . . Haapala, K. R. (2019). Knowledge-based design of artificial neural network topology for additive manufacturing process modeling: a new approach and case study for fused deposition modeling. *Journal of Mechanical Design, 141*(2), 021705.
Nasereddin, J. M., Wellner, N., Alhijjaj, M., Belton, P., & Qi, S. (2018). Development of a simple mechanical screening method for predicting the feedability of a pharmaceutical FDM 3D printing filament. *Pharmaceutical research, 35*(8), 1-13.
Ouhsti, M., El Haddadi, B., & Belhouideg, S. (2018). Effect of printing parameters on the mechanical properties of parts fabricated with open-source 3D printers in PLA by fused deposition modeling. *Mechanics and Mechanical Engineering, 22*(4), 895-907.
Pandzic, A., Hodzic, D., & Milovanovic, A. (2019). EFFECT OF INFILL TYPE AND DENSITY ON TENSILE PROPERTIES OF PLAMATERIAL FOR FDM PROCESS. *Annals of DAAAM & Proceedings, 30*.
Parulski, C., Jennotte, O., Lechanteur, A., & Evrard, B. (2021). Challenges of fused deposition modeling 3D printing in pharmaceutical applications: Where are we now? *Advanced Drug Delivery Reviews, 175*, 113810.

Patil, P., Singh, D., Raykar, S. J., & Bhamu, J. (2021). Multi-objective optimization of process parameters of Fused Deposition Modeling (FDM) for printing Polylactic Acid (PLA) polymer components. *Materials Today: Proceedings, 45*, 4880-4885.

Pazhamannil, R. V., Govindan, P., & Sooraj, P. (2021). Prediction of the tensile strength of polylactic acid fused deposition models using artificial neural network technique. *Materials Today: Proceedings, 46*, 9187-9193.

Prakash, C., Singh, G., Singh, S., Linda, W., Zheng, H., Ramakrishna, S., & Narayan, R. (2021). Mechanical reliability and in vitro bioactivity of 3D-printed porous polylactic acid-hydroxyapatite scaffold. *Journal of Materials Engineering and Performance, 30*(7), 4946-4956.

Raykar, S. J., & D'Addona, D. (2020). Selection of best printing parameters of fused deposition modeling using VIKOR. *Materials Today: Proceedings, 27*, 344-347.

Sachs, E. M., Haggerty, J. S., Cima, M. J., & Williams, P. A. (1993). Three-dimensional printing techniques. In: Google Patents.

Sheoran, A. J., & Kumar, H. (2020). Fused Deposition modeling process parameters optimization and effect on mechanical properties and part quality: Review and reflection on present research. *Materials Today: Proceedings, 21*, 1659-1672.

Short, D. B. (2015). Use of 3D printing by museums: educational exhibits, artifact education, and artifact restoration. *3D Printing and Additive Manufacturing, 2*(4), 209-215.

Singh, D., Babbar, A., Jain, V., Gupta, D., Saxena, S., & Dwibedi, V. (2019). Synthesis, characterization, and bioactivity investigation of biomimetic biodegradable PLA scaffold fabricated by fused filament fabrication process. *Journal of the Brazilian Society of Mechanical Sciences and Engineering, 41*(3), 1-13.

Singh, G., Singh, S., Prakash, C., Kumar, R., Kumar, R., & Ramakrishna, S. (2020). Characterization of three-dimensional printed thermal-stimulus polylactic acid-hydroxyapatite-based shape memory scaffolds. *Polymer Composites, 41*(9), 3871-3891.

Singh, S., Prakash, C., & Ramakrishna, S. (2019). 3D printing of polyether-ether-ketone for biomedical applications. *European Polymer Journal, 114*, 234-248.

Song, P., Zhou, C., Fan, H., Zhang, B., Pei, X., Fan, Y., . . . Dong, Z. (2018). Novel 3D porous biocomposite scaffolds fabricated by fused deposition modeling and gas foaming combined technology. *Composites Part B: Engineering, 152*, 151-159.

Teharia, R., Singari, R. M., & Kumar, H. (2021). Optimization of process variables for additive manufactured PLA based tensile specimen using taguchi design and artificial neural network (ANN) technique. *Materials Today: Proceedings*.

Trivedi, A., & Gurrala, P. K. (2021). Fuzzy logic based expert system for prediction of tensile strength in Fused Filament Fabrication (FFF) process. *Materials Today: Proceedings, 44*, 1344-1349.

Xu, Z., Fostervold, R., & Razavi, S. M. J. (2021). Thickness effect on the mechanical behavior of PLA specimens fabricated via Fused Deposition Modeling. *Procedia Structural Integrity, 33*, 571-577.

Yadav, D., Chhabra, D., Garg, R. K., Ahlawat, A., & Phogat, A. (2020). Optimization of FDM 3D printing process parameters for multi-material using artificial neural network. *Materials Today: Proceedings, 21*, 1583-1591.